

SIMULATION OF HIGH POWER LASERS

**Timothy J. Madden
Robert K. Decker**

1 June 2010

Technical Paper

Approved for public release; distribution unlimited.



**AIR FORCE RESEARCH LABORATORY
Directed Energy Directorate
3550 Aberdeen Ave SE
AIR FORCE MATERIEL COMMAND
KIRTLAND AIR FORCE BASE, NM 87117-5776**

REPORT DOCUMENTATION PAGE				Form Approved OMB No. 0704-0188	
Public reporting burden for this collection of information is estimated to average 1 hour per response, including the time for reviewing instructions, searching existing data sources, gathering and maintaining the data needed, and completing and reviewing this collection of information. Send comments regarding this burden estimate or any other aspect of this collection of information, including suggestions for reducing this burden to Department of Defense, Washington Headquarters Services, Directorate for Information Operations and Reports (0704-0188), 1215 Jefferson Davis Highway, Suite 1204, Arlington, VA 22202-4302. Respondents should be aware that notwithstanding any other provision of law, no person shall be subject to any penalty for failing to comply with a collection of information if it does not display a currently valid OMB control number. PLEASE DO NOT RETURN YOUR FORM TO THE ABOVE ADDRESS.					
1. REPORT DATE (DD-MM-YYYY) 01 June 2010		2. REPORT TYPE Technical Paper		3. DATES COVERED (From - To) 01 June 2008 – 31 May 2010	
4. TITLE AND SUBTITLE Simulation of High Power Lasers (Preprint)				5a. CONTRACT NUMBER In-House (DF297846)	
				5b. GRANT NUMBER	
				5c. PROGRAM ELEMENT NUMBER 62605F	
6. AUTHOR(S) Timothy J. Madden Robert K. Decker				5d. PROJECT NUMBER 4866	
				5e. TASK NUMBER LB	
				5f. WORK UNIT NUMBER 21	
7. PERFORMING ORGANIZATION NAME(S) AND ADDRESS(ES) Air Force Research Laboratory/RDLC 3550 Aberdeen Avenue SE Kirtland AFB, NM 87117-5776		8. PERFORMING ORGANIZATION REPORT NUMBER			
9. SPONSORING / MONITORING AGENCY NAME(S) AND ADDRESS(ES) Air Force Research Laboratory 3550 Aberdeen Avenue SE Kirtland AFB, NM 87117-5776		10. SPONSOR/MONITOR'S ACRONYM(S)			
		11. SPONSOR/MONITOR'S REPORT NUMBER(S) AFRL-RD-PS-TP-2010-1016			
12. DISTRIBUTION / AVAILABILITY STATEMENT Distribution for public release; distribution is unlimited.					
13. SUPPLEMENTARY NOTES Submitted for publication in Proceedings of the DoD High Performance Computing Modernization Program User Group Conference 2010, June 14 – 18, 2010, Schaumburg, IL. PA approval case number: 377 ABW-2010-0944. Government Purpose Rights.					
14. ABSTRACT: The time-dependent, chemically reacting, viscous fluid dynamics within gas laser mixing systems and pressure recovery systems are simulated using the unsteady, laminar and turbulent multi-component Navier-Stokes equations. The solutions of these equations are generated within simulations of the relevant laser sub-systems at standard operating conditions. The simulations are performed to provide greater insight regarding the physical processes underlying these sub-systems so that these physics may be exploited to improve performance. In this light, simulations of several laser subsystems are provided.					
15. SUBJECT TERMS Lasers, chemical oxygen-iodine laser, supersonic diffuser, computational fluid dynamics, chemically reacting flows, high performance computing, parallel scaling performance.					
16. SECURITY CLASSIFICATION OF:			17. LIMITATION OF ABSTRACT SAR	18. NUMBER OF PAGES 20	19a. NAME OF RESPONSIBLE PERSON Timothy J. Madden
a. REPORT Unclassified	b. ABSTRACT Unclassified	c. THIS PAGE Unclassified			19b. TELEPHONE NUMBER (include area code) 505-846-9076

Standard Form 298 (Rev. 8-98)
Prescribed by ANSI Std. Z39.18

THIS PAGE INTENTIONALLY LEFT BLANK

Simulation of High Power Lasers

Timothy J. Madden

*Air Force Research Laboratory Directed Energy Directorate,
Kirtland Air Force Base, NM 87117-5776*

and

Robert K. Decker

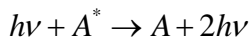
*Air Force Academy, Department of Aeronautical and Aerospace Engineering,
Colorado Springs, CO 80840*

1. Introduction.

Gas lasers are complex, energy conversion devices that utilize two-phase chemistry, fluid dynamics, and optics to convert the bond energy within fuels to coherent radiation capable of projecting high energy very large distances at the speed of light. Given the complexity of the interactions between the various physical processes, simulation of chemical lasers presents an obvious opportunity to apply high performance computing and facilitate understanding and optimization of these devices. The work show here illustrates the application of high performance computing to achieve an increased understanding of the physics underlying lasers and improve their operation. Computational fluid dynamic (CFD) simulations for the chemically reacting COIL flowfield are executed to achieve these goals.

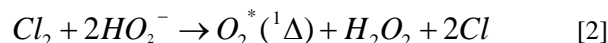
2. Problem and Methodology.

Gas lasers, such as chemical oxygen iodine lasers (COILs) operate on a series of exothermic, gas phase chemical reactions that create a population inversion, or non-Boltzmann energy distribution, within the energy states of the products of reactions. As these products equilibrate towards a Boltzmann distribution of energy states, photons are emitted via spontaneous emission. If an energetically excited species A^* emits a photon of energy $h\nu$ during the equilibration process, then this photon may collide with another excited species A^* causing it to release another photon with equal energy in the same direction of propagation as the first photon. This can be described as:

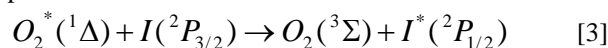


As the number of photons increases, a wave builds within the gas that is directed and controlled by mirrors that transmit a fraction of the photons with each reflection of the optical waves. As the wave builds within the gas, the increase in the number of photons or the wave intensity per given unit distance leads to the concept of wave amplification or laser gain. Gain is a key performance parameter in chemical lasers and is frequently referred to in this work. A COIL produces the

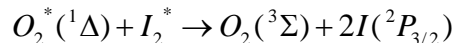
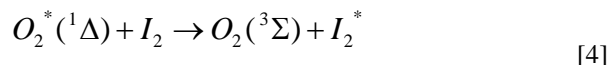
excited lasing species A^* via a complex series of chemical reactions, both liquid and gas phase. The first phase occurs in liquid, and generates the ‘fuel’ via the reaction:



The electronically excited singlet-delta state of oxygen diffuses out of the liquid and is picked up by a carrier gas, usually He. COILs use $O_2(^1\Delta)$ collisions with ground state I atoms, $I(^2P_{3/2})$, to efficiently generate the lasing species $I(^2P_{1/2})$ via the energy transfer process:



This reaction is more efficient at producing $I(^2P_{1/2})$ than any other known process, hence the reason a more direct reaction path to $I(^2P_{1/2})$ is not used. An additional reactive process occurs in COIL where $O_2(^1\Delta)$ dissociates molecular iodine, I_2 , to generate the ground state I atoms, $I(^2P_{3/2})$. This multi-step energy transfer/reactive process occurs through the following reactions:



The exact state(s) of I_2 that I_2^* represents is still a point of contention amongst researchers at this time due to the considerable difficulty in constructing experiments to clearly identify and track multiple vibrational and electronic excited states. Because of the indeterminate nature of the I_2^* state(s) and the number of potential intermediate energy transfer processes involved, mathematical constructs are used to describe equation [4] but the construct is fitted to experimental measurements of the overall rate of dissociation of I_2 .

Given the multiple chemical species and states within the COIL flowfield, the gas flow within COILs can be generally described as the flow of particles of different chemical composition with collisional interactions occurring between the particles and between the particles and the photons within the radiation field. Mathematically, this flow of particles is treated as a continuum and is approximated by the Navier-Stokes

continuity equations for mass, momentum, and energy. In integral form, these equations are given by:

$$\begin{aligned} \frac{\partial}{\partial t} \iiint_{vol} \langle Q \rangle dvol + \oint_A (\vec{F} - \vec{F}_v) \cdot \hat{n} dA \\ = \iiint_{vol} \langle S \rangle dvol \end{aligned} \quad [5]$$

where $\langle Q \rangle$ is the vector of the cell averaged conserved quantities of species density, momentum component, and pressure; \vec{F} and \vec{F}_v are the inviscid and viscous fluxes of the conserved quantities at the cell boundary, and $\langle S \rangle$ is the vector of cell averaged sources of the conserved quantities. Contained within these equations are descriptions for the rates of production and loss of reacting species, the production and absorption of photons, energy transfer within different modes in the molecules, molecular mixing, and temporal variation. Reynolds numbers vary from order 1000 in the mixing system to 40,000 in the supersonic diffuser of the COIL flowfield. The low Reynolds number simulations for the mixing nozzles are performed with no turbulence closure, and can be considered to be similar in nature to Direct Navier-Stokes simulations. Turbulence closure formulations are added to the Navier Stokes equations in the context of Reynolds Averaging for the diffuser simulations. The low Reynolds number variant of the Wilcox $k-\omega$ model,¹ the Menter Shear Stress Transport (SST),² and the Wilcox Stress-Omega³ formulation of the Reynolds Stress model are investigated here for the diffuser application. The computational fluid dynamics (CFD) code GASP from AeroSoft Inc. is employed to solve these equations for the simulations performed here.

Reacting flow, i.e. COIL, and non-reacting flow simulations of experiment hardware are performed in this work. The GASP COIL model utilizes separate species mass conservation equations for each of the chemically reacting components of the COIL flow in addition to the base conservation equations for momentum and energy. An effective binary diffusion model is used to describe concentration and pressure contributions to mass diffusion, an important process in the low density COIL flowfield.

An experiment consisting of a supersonic (M~2.2) converging-diverging nozzle section with secondary mass injection in the nozzle expansion downstream of the throat, followed by a supersonic diffuser section and a subsonic diffuser was simulated here. In the experiments, the pressures, temperatures, and massflows are fixed while the back pressure at the subsonic diffuser exit is varied. The primary flow consists of He and O₂ at 4:1 molar flow ratios and the secondary flow of He and N₂ at a 8.3:1 ratio with the N₂ flow simulating the use of I₂ in chemical oxygen-iodine laser (COIL) flowfields.

The primary flow enters at 65 torr and 300 K total conditions and the secondary flow set to achieve full penetration in this flow. The back pressure at the subsonic diffuser exit is varied from 14 through 29.5 torr. The diffuser experiment apparatus simulated here is shown in Figures 1 and 2.

The GASP model for the diffuser experiment utilizes a computational grid used consisting of 659 blocks and 33.5 million grid cells. The computational domain that this grid discretizes consists of half the experimental flow channel in the lateral (Z) direction. As temperatures are sufficiently low, no chemical reactions are assumed to be ongoing between the species in this flow and it is treated as non-reacting. Boundary conditions accomplish the symmetry approximation through the enforcement of planar symmetry at the centerline in the lateral direction. No-slip 300 K temperature boundary conditions are used at the wetted surfaces of the nozzle and injector orifices. The nozzle and injector subsonic inflow boundary conditions fix the total pressure, total temperature, and the species fractions at constant values, while the derivative of the static pressure is set to 0. The outflow boundary condition at the subsonic diffuser exit sets the static pressure to a fixed value, and is set to the measured value for each of the experiments simulated here. 3 species mass conservation equations corresponding to the components of the gases used in the experiment in addition to the base conservation equations for momentum and energy and 2 turbulent closure equations for the $k-\omega$ based models. In the case of the Stress-Omega simulations, 6 turbulent closure equations are solved.

The GASP model for the mixing nozzle simulations utilizes a computational grid consisting of 18 blocks and 9.3 million grid cells. The computational domain which this grid discretizes represents the smallest geometrically similar element of a repeating pattern of elements within the COIL experiment flowfield hardware, denoted a ‘unit-domain.’ The unit-domain consists of a section of a supersonic (M~2.2) converging-diverging slit nozzle with one large and two small orifices that inject reactants into the primary flow passing through this nozzle. The orifices introduce a sonic mixture of He and I₂ into the subsonic primary flow composed of He, O₂(¹Δ), O₂(³Σ), H₂O, and Cl₂ inducing complex, time dependent, 3-D flow structure as the jet interacts with the crossflow. It is the combination of the interfacial area created by the complex flow structure and molecular diffusion that mixes the two flows. Boundary conditions generate the unit-domain approximation structure through the enforcement of planar symmetry at the nozzle centerline in the vertical direction and periodicity on the side boundaries in the lateral direction that allows fluxes from one surface to pass through its’ opposite boundary across the domain and vice-versa. No-slip constant temperature

boundary conditions are used at the wetted surfaces of the nozzle and orifices, with the temperature fixed at 400 K at the orifice region walls and 300 K at the nozzle walls. The nozzle and injector subsonic inflow boundary conditions fix the total pressure, total temperature, and the species fractions at constant values, while the derivative of the static pressure is set to 0. The nozzle outflow boundary condition sets the second derivative of the dependent variables to 0 as is appropriate for supersonic flows. The COIL chemistry is described either using a 13 species, 52 reaction finite-rate mechanism⁴ that models the gas phase chemical kinetic processes generating the population inversion in atomic iodine necessary for laser oscillation. Power extraction from this flow is captured using a ray trace, geometric optics model that captures the physical coupling between the light resonance in the laser cavity and the energy state distribution in the excited states in the flow traversing the resonator region of the supersonic expansion. References providing additional details regarding the application of GASP to this problem may be found in Madden et al.^{5,6} and Eppard et al.⁷

3. Results.

The simulations were executed with time steps varying between $1 \cdot 10^{-8}$ and $1 \cdot 10^{-3}$ sec, with convergence of 3 orders of magnitude obtained in the Menter SST and Stress-Omega cases. The laminar and low Re $k-\omega$ simulations demonstrated oscillatory behavior and did not converge beyond 1.5 orders of magnitude. The lack of convergence in these cases is associated with the complexity of the interaction between the key elements of the fluid physics in this flowfield, namely the compressibility, the boundary layer, turbulence, and the back pressure of the subsonic diffuser. As the back pressure is increased above that associated with the area ratio relative to the choke point, the force associated with this pressure overcomes the low momentum regions in the boundary layer and stagnates or reverses the boundary layer, further thickening it. As the boundary layer thickens with the upstream propagation of the back pressure, the area of the core flow is decreased, the Mach number decreased in the supersonic regions, and the pressure increased. A process of dynamic equilibration is established, with the core flow pressure adjusting to the boundary layer thickening. Turbulence plays a key role here as the much smaller boundary layer thickness of the turbulent boundary tends to inhibit upstream propagation of the back pressure, a positive effect in the case of gas lasers as this serves to isolate the supersonic cavity region between the nozzle expansion and the supersonic diffuser. Further adding to the complexity are the low Reynolds numbers in these low density flows, with Re_x reaching order 40,000 based on the wall length in the constant angle expansion region of the

nozzle. Turbulent transition will be associated with shock wave reflections and adverse pressure gradients, and may be intermittent with laminarization occurring between events. Figs. 2 and 3 illustrate the general flow structure showing the extensive flow disruption that occurs to the smooth, regular flow structure associated with the injected fluid as the boundary layer enlarges responding to the upstream influence of the exit's overpressure, as well as the oblique shock structure superimposed upon the secondary injection process.

Four sets of simulations were performed corresponding to the turbulent closure assumption used: laminar, and turbulent with low Re $k-\omega$, Menter SST, and Stress-Omega. Each set of simulations used 4 separate back pressures at the outflow boundary: 14.7, 22.8, 26.4, and 29.5 torr. Wall pressures were extracted from each simulation at the locations of the pressure taps from the experiment; little difference was found to occur between the locations laterally or from top to bottom, so comparisons here focus on the column in the streamwise direction on the upper wall along the lateral centerline of the experiment. Figs. 5 – 8 compare the four sets of simulations with the experiment data at the various back pressures. Observing the experiment wall pressure data across these figures, the wall pressure is seen to drop with the nozzle expansion and then undergo either a gradual increase in the case of the 14.7 torr back pressure experiment, or a somewhat abrupt pressure increase in the 22.8, 26.4, and 29.5 torr experiments, then transitioning toward the back pressure through the supersonic and subsonic diffusers. The more gradual pressure increase in the 14.7 torr experiment is associated with the recovery in the supersonic diffuser transitioning to the near back pressure matching conditions in the subsonic diffuser. The abrupt pressure rise in the 22.8, 26.4, and 29.5 torr experiments, however, is associated with the upstream propagation of the back pressure through the boundary layer and the corresponding increase in the boundary layer thickness causing core flow area decreases, Mach number decreases, and pressure increases. Thus, in the 14.7 torr experiment the supersonic diffuser prevents upstream encroachment of the back pressure and in the higher back pressures it is overwhelmed. *A priori* to examining the simulation results, sidewall boundary layer thickness and turbulence prediction would be expected to correlate with wall pressure prediction.

Examination of the simulation wall pressure predictions indicates that the general trend is that the laminar and low Re $k-\omega$ simulations tend to have very poor prediction of the wall pressures and the Menter SST and Stress-Omega models have somewhat better capture, with the Menter SST best overall. Taking the 14.7 torr case as an example, the wall pressures rise starts at the 0.15 m station in the laminar simulation and at the 0.20

m station in the low Re $k-\omega$ simulation, 0.15 to 0.20 m upstream of the supersonic diffuser entrance where a more gradual pressure rise starts in the Menter SST and Stress-Omega cases. The pressure increase much further upstream in the laminar and low Re $k-\omega$ simulations indicates that these simulations have thicker boundary layer predictions and greater susceptibility to upstream pressure propagation. The observation for the 14.7 torr case is repeated in the high back pressure cases in Figs. 6 – 8, with continued wall pressure rises for the laminar and low Re $k-\omega$ simulations upstream of the Menter SST and Stress-Omega simulations as well as the experiment data, and generally poor wall pressure predictions.

The case with the Menter SST and Stress-Omega simulations is different, however. In the 14.7 torr case in Fig. 5, the Stress-Omega performs slightly better than the Menter SST, but in the 22.8, 26.4, and 29.5 torr cases in Figs. 6 – 8 the Menter SST model performs considerably better. Given the previous example with the laminar and low Re $k-\omega$ simulations, the reasons for these differences would appear to lie in the boundary layer predictions, most specifically in the turbulence production as this dictates the strength of the turbulence and momentum mixing with the freestream that in turn dictates the boundary layer thickness prediction. To examine turbulence production, the ratio of turbulence production to dissipation is plotted for the Menter SST and Stress-Omega simulations at locations in and around the pressure increase associated with the further most upstream influence of the back pressure upstream. Figs. 9 – 14 show this ratio as well as the corresponding streamwise momentum (ρu) distribution at the same locale. In Figs. 9 and 10, the production to dissipation ratio and streamwise momentum are shown in a transverse plane (y, z) toward the end of the nozzle upstream of the supersonic diffuser entrance. The Menter SST and Stress-Omega simulations predict similar distributions and magnitudes of these quantities at this location. However, instead of turbulence production occurring adjacent to the side and upper walls, it only occurs adjacent to the upper and lower walls, suggesting that turbulent production in this flow is triggered by vorticity introduced with the secondary injection along the upper and lower surfaces. The sidewalls and corners then become avenues for the back pressure to propagate upstream through the larger regions of laminar, subsonic flow found there. Further downstream in the supersonic diffuser within the pressure rise, shown in Figs. 11 and 12, the predicted turbulent production distribution is somewhat different for the Menter SST model as compared to the Stress-Omega model, with greater freestream turbulence production in the Menter SST model. While there does not appear to be a significant affect from the freestream turbulence, the differences in the turbulent production

near the walls lead to somewhat larger low momentum regions in the Menter SST model prediction, hence leading to higher pressures. This trend continues further downstream in Figs. 13 and 14 with the Menter SST model continuing to predict larger low momentum regions and smaller core flows. In the case of this back pressure, the Menter SST model predicts higher pressures than the Stress-Omega model and is not as accurate in predicting the wall pressures.

The comparison changes for the higher back pressure cases at 22.8, 26.4, and 29.5 torr, as was indicated previously in Figs. 6 -8. The Menter SST model captures the location approximately the same to slightly better than the Stress-Omega model, but also captures the pressure rise substantially better. The trend that is borne out in Figs. 15 – 32 is that while the Menter SST and Stress-Omega models have similar turbulence production to dissipation ratio profiles upstream of the pressure rise, downstream within the pressure rise the Menter SST model predicts a decrease in the turbulence production to dissipation ratio relative to both the upstream values and the Stress-Omega model. The decrease in the turbulence production leads to thicker boundary layers and smaller core flows, leading to higher pressures. Figs. 18, 20, 24, 26, 30, and 32 illustrate this point, with the larger low momentum regions becoming increasingly pronounced in the Menter SST simulations relative to the Stress-Omega counterparts for the region within the pressure rise both with increasing distance downstream and with increasing back pressure. Conversely, the higher turbulence production downstream of the pressure rise with the Stress-Omega model leads to more rapid momentum mixing and thinner boundary layers, resulting in larger core flow areas and lower pressures. Thus, the advantage for the Menter SST model in its' physical prediction capability lies not just with higher turbulence production to dissipation upstream, improving the capture of the location of the pressure rise due to the back pressure upstream influence, but also with the decrease in the turbulence production to dissipation ratio downstream within the pressure rise leading to more accurate capture of the pressure increase.

Initial simulations examining the coupling between flow structure, reactant mixing, chemical reaction, gain production, and laser power extraction within a COIL mixing nozzle were performed using the GASP mixing nozzle model described in Section 3. Two separate methods of temporal execution of the GASP model were employed for comparison. The first utilizes a comparatively large time step of $1 \cdot 10^{-3}$ sec in conjunction with a time step limiting scheme to stabilize the execution with local decreases in the time step in regions where instabilities are identified. The scheme allows for more rapid evaluation with the larger time

step, but does result in the loss of flow structure having smaller time scales of evolution. These same flow structures can be associated with the very mixing of reactants that drives lasing in COILs. The second scheme investigated is a time accurate scheme using a time step of $1 \cdot 10^{-8}$ sec. This approach directly tracks the temporal evolution of the flow structures previously identified to occur at timescales as small as $1 \cdot 10^{-6}$ sec.^{8,9} Fig. 33 illustrates the coupling between the flow structure, laser gain, and laser intensity field. Particularly evident is the dramatic decrease in laser gain as the intensity field achieves equilibrium between the amount of energy pulled from the flow into the recirculating optical field in the resonator and the amount of light transmitted out through the laser mirrors.

The question of differences in flow structure is particularly evident in Figs. 34 and 35, showing an 2-D cut of the gain field from the large and small time step simulations. The large time step simulation illustrates smoothing of flow structures and an absent of the smaller scale structures that are evident in the small time step simulation. Additionally, peak gains are slightly higher in the large step simulation as compared with the small time step simulation. The differences in flow structure and gain distribution translate into differences in the optical field as captured by the ray trace model. Figs. 36 and 37 show normalized intensity distributions from a single time step for the large and small time step simulations. It is readily apparent that the differences in flow structure translate into differences in the intensity field captured within the simulations. Future work will examine in detail the impact of these differences upon power predictions.

The parallel performance of GASP on the various platforms relevant to this proposal for a wide variety of 3-D Navier-Stokes simulations on grids ranging from 2 to 32 million grid cells and with 3 to 18 species is shown in Fig. 12. Load balancing efficiency for all cases was between 97.7 and 99.9% and communications costs varied from 25% to 12%. The resulting scaling efficiencies are between 70% and 88% with the exception being 2 heavily loaded cases on the SGI 4700 with un-optimized code at 55%. The communications costs are directly attributable to the use of fully implicit integration, which requires communication of zonal boundary information after each inner-iteration of the Gauss-Seidel or Jacobi matrix solver. Each speedup number is generated for an optimal decomposition of the computational domain for the given number of processors. As is indicated, the speed-ups are linear through 1024 processors with drop-offs in efficiency occurring above 1280 processors. As is typical with the domain decomposition model used by GASP for parallel execution, memory use decreases as the number of processors used increases, and is easily tuned to utilize

the memory available on the execution nodes for the computational platform of interest.

4. Summary

The analysis performed here provides important information relevant to the simulation of high energy gas lasers. The supersonic diffuser work clearly illustrates the challenge of simulating turbulent flows using statistical turbulence models. While the low Re variant of the Wilcox turbulence model was found to be entirely inadequate for this type of analysis, even turbulence models such as the Menter SST and the Stress-Omega which were anticipated to provide superior performance were found to not capture the essential physics for the variety of operating conditions examined. From this standpoint, higher order methods such as large eddy simulation (LES) or DNS may be necessary for these types of flows.

The mixing nozzle simulations provide an initial examination of possible approaches for simulating power extraction in COILs. Differences in the flow structure were found to exist comparing large and small time step approaches to simulation. These differences, attributed to capture of fine scale flow structure associated with small time scales, resulted in differences in the prediction of laser gain and laser intensity in the simulation. Future work will examine the impact of these predictions on the end product of laser power.

5. References

- ¹ Wilcox, D. C., *Turbulence Modeling for CFD*, DCW Industries, Inc. pp. 185-193, July 1998.
- ² Menter, F. L., "Improved two-equation k-omega turbulence models for aerodynamic flows," *NASA Technical Memorandum 103975*, October 1992.
- ³ Wilcox, D. C., *Turbulence Modeling for CFD*, DCW Industries, Inc. pp. 294-296, July 1998.
- ⁴ Perram, G. P., *Int. J. Chem. Kinet.* **27**, 817-28 (1995).
- ⁵ Madden, T. J. and Solomon, W. C., AIAA 97-2387, 28th Plasmadyamics and Lasers Conference, Atlanta, GA, June 23-25, 1997.
- ⁶ Madden, T.J., *SPIE Proceedings of XIV International Symposium On Gas Flow & Chemical Lasers and High Power Laser Conference*, Wroclaw, Poland, 25-30 August, 2002.
- ⁷ W. M. Eppard, W. D. McGrory, A. G. Godfrey E. M. Cliff, and J. T. Borggaard, "Recent advances in numerical techniques for the design and analysis of COIL systems," AIAA-2000-2576, AIAA 31st Plasmadyamics and Lasers Conference, Denver, CO, June 19-22, 2000.
- ⁸ Madden, T. J. "An Analysis of Mechanisms Underlying Flow Unsteadiness in Chemical Oxygen-Iodine Laser Mixing Systems," AIAA-2005-5390, 36th AIAA

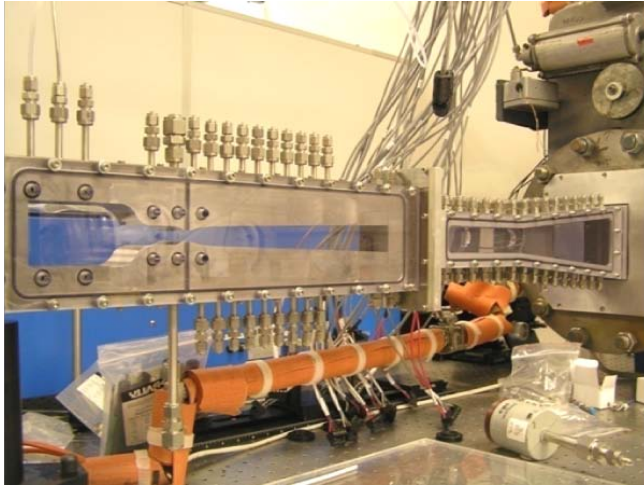


Figure 1. Supersonic nozzle and diffuser experiment hardware simulated in this work. The flow is from left to right with the nozzle plenum on the far left and the flange at the subsonic diffuser exit at the far right.

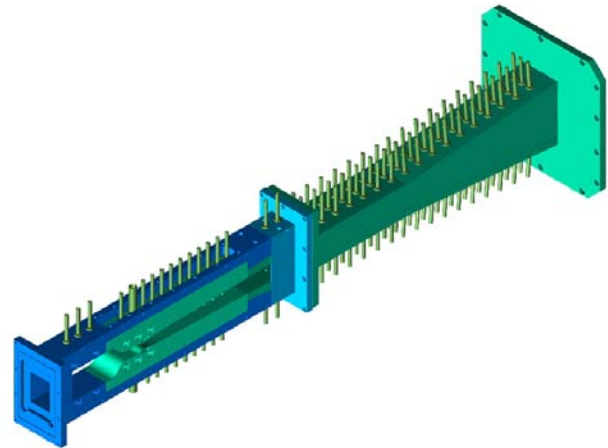


Figure 2. 3-D isoview of the CAD layout for the experiment hardware. Wetted surfaces were extracted from this drawing and imported into Gridgen for grid generation.

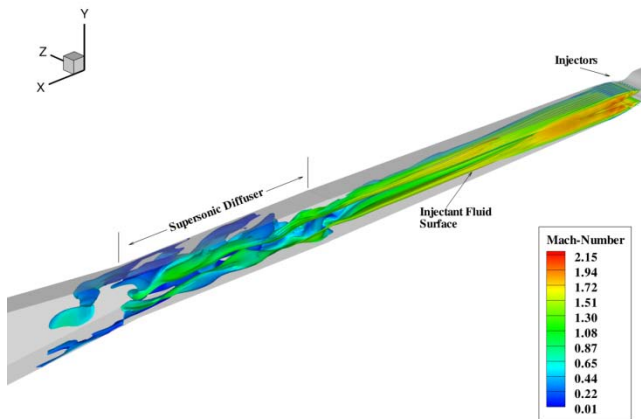


Figure 3. Mach number contours superimposed an isosurface of constant N_2 mole fraction, tracing the flow from the injectors and illustrating the effect of the back pressure propagation upstream upon the core flow structure. Note the disruption in the core flow that extends upstream of the supersonic diffuser entrance.

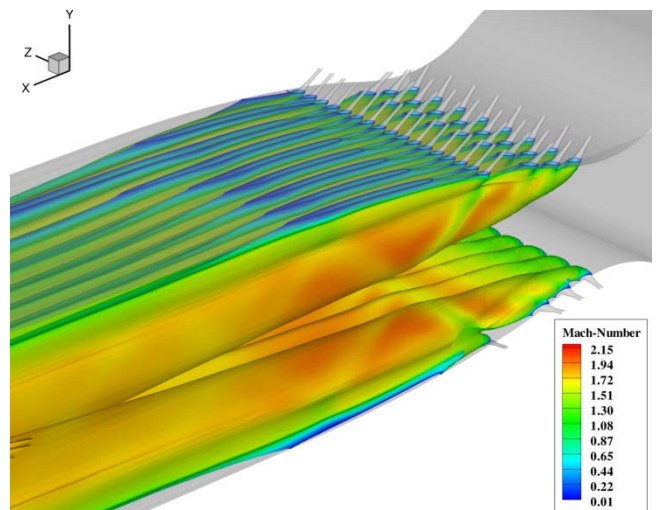


Figure 4. Close-up view of the injector region from Fig. 3 highlighting the flow structure and the oblique shock pattern that arises in the supersonic region of the flowfield.

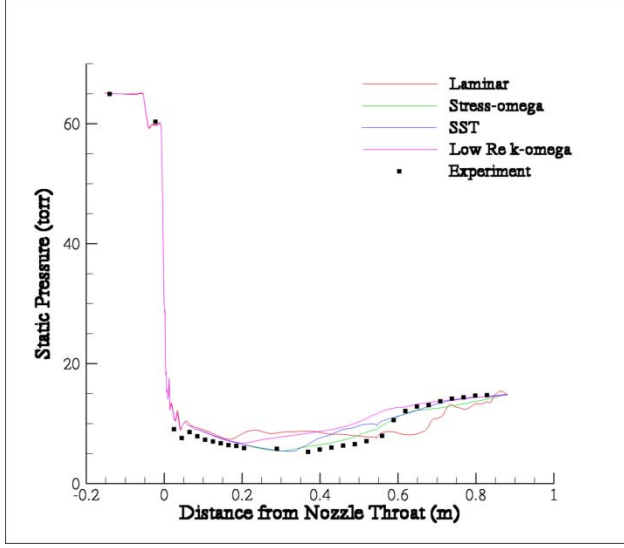


Figure 5. Comparison of wall pressures from the experiment with those from the laminar, low Re $k-\omega$, Menter SST, and Stress-Omega at the lateral centerline of the upper wall, with the back pressure at 14.7 torr.

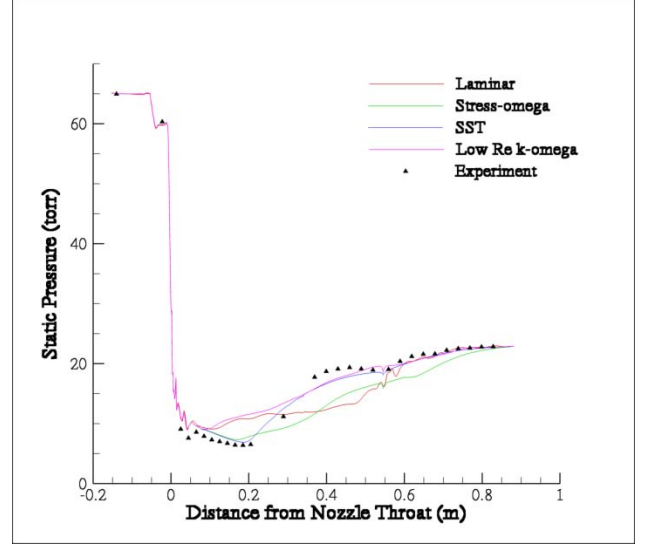


Figure 6. Comparison of wall pressures from the experiment with those from the laminar, low Re $k-\omega$, Menter SST, and Stress-Omega at the lateral centerline of the upper wall, with the back pressure at 22.8 torr.

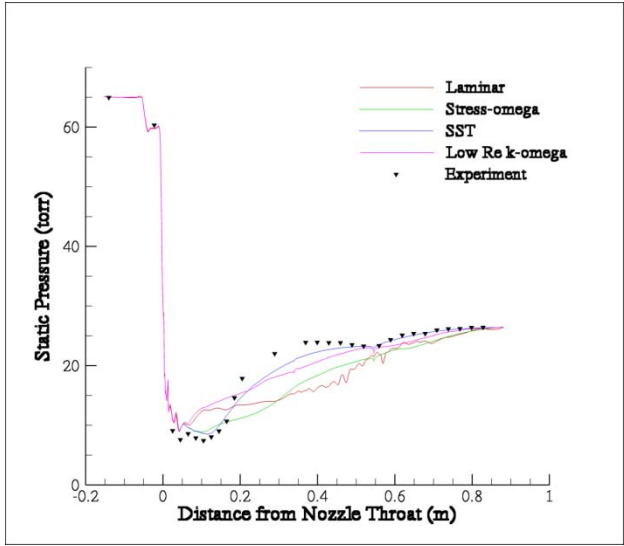


Figure 7. Comparison of wall pressures from the experiment with those from the laminar, low Re $k-\omega$, Menter SST, and Stress-Omega at the lateral centerline of the upper wall, with the back pressure at 26.4 torr.

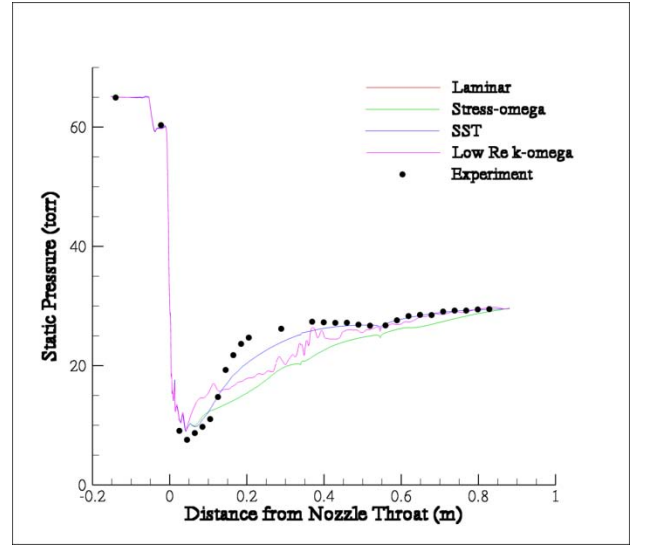


Figure 8. Comparison of wall pressures from the experiment with those from the laminar, low Re $k-\omega$, Menter SST, and Stress-Omega at the lateral centerline of the upper wall, with the back pressure at 29.5 torr.

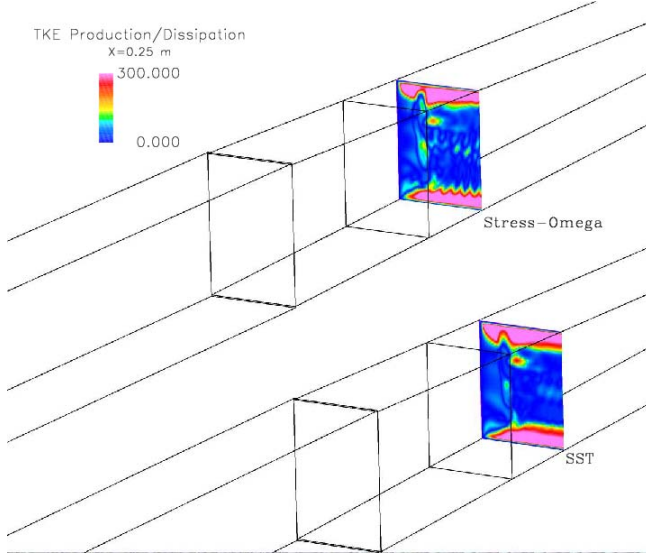


Figure 9. Comparison of the turbulent kinetic energy production to dissipation ratio predictions from the Stress-Omega and Menter SST simulations with a back pressure of 14.7 torr at a location just upstream of the start of the pressure rise.

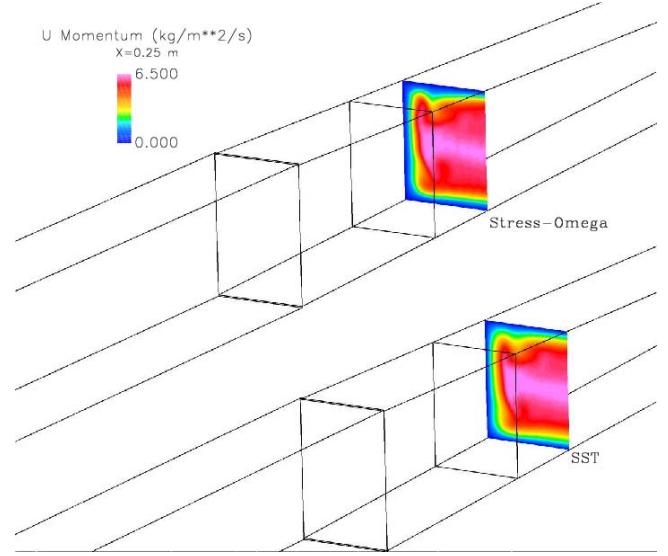


Figure 10. Comparison of the U momentum (ρu) prediction from the Stress-Omega and Menter SST simulations with a back pressure of 14.7 torr at a location just upstream of the start of the pressure rise.

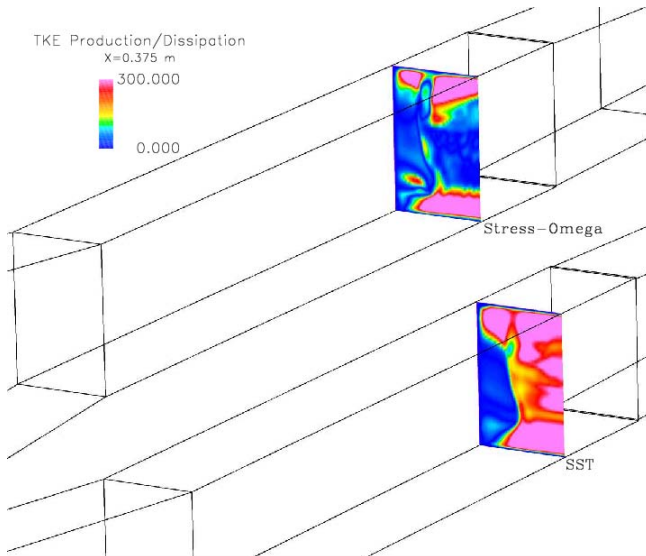


Figure 11. Comparison of the turbulent kinetic energy production to dissipation ratio predictions from the Stress-Omega and Menter SST simulations with a back pressure of 14.7 torr at a location just downstream of the start of the pressure rise.

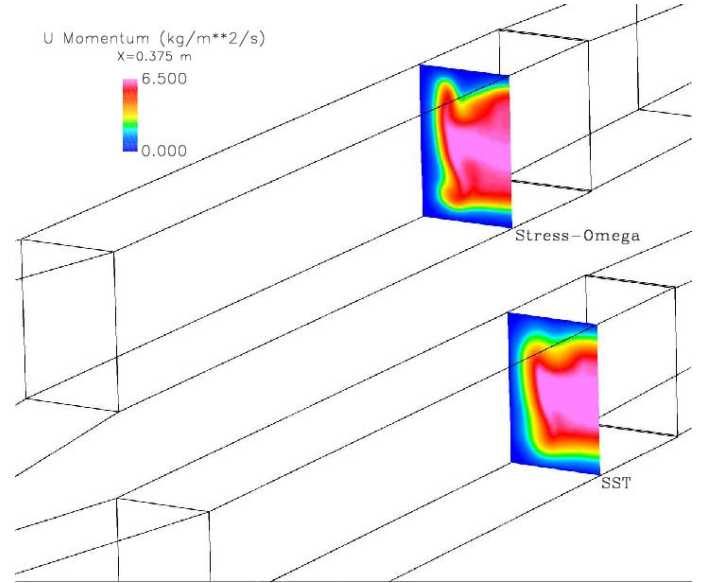


Figure 12. Comparison of the U momentum (ρu) prediction from the Stress-Omega and Menter SST simulations with a back pressure of 14.7 torr at a location just downstream of the start of the pressure rise.

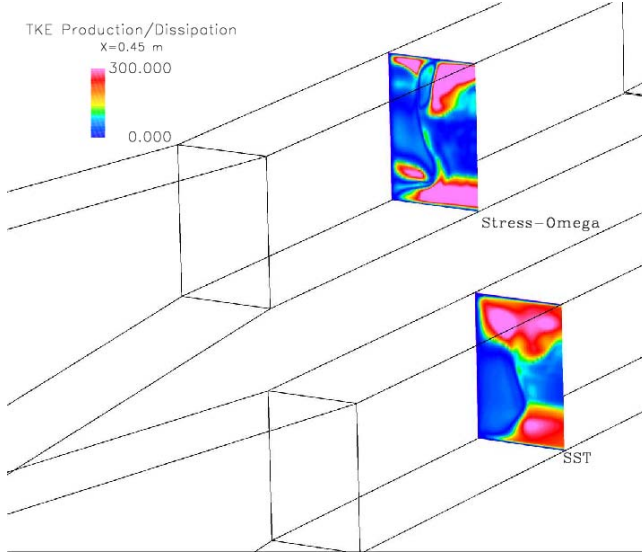


Figure 13. Comparison of the turbulent kinetic energy production to dissipation ratio predictions from the Stress-Omega and Menter SST simulations with a back pressure of 14.7 torr at a location near the end of the pressure rise.

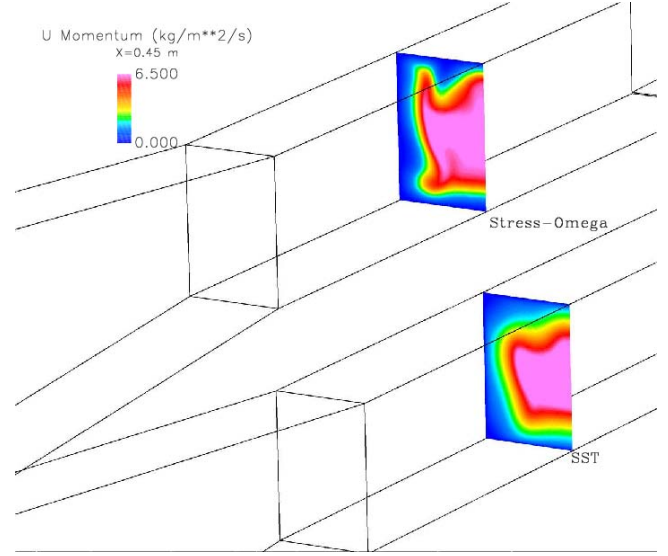


Figure 14. Comparison of the U momentum (ρu) prediction from the Stress-Omega and Menter SST simulations with a back pressure of 14.7 torr at a location near the end of the pressure rise.

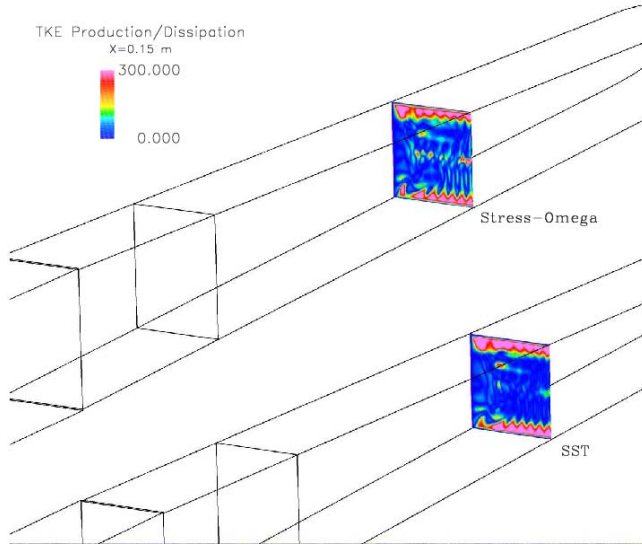


Figure 15. Comparison of the turbulent kinetic energy production to dissipation ratio predictions from the Stress-Omega and Menter SST simulations with a back pressure of 22.8 torr at a location just upstream of the start of the pressure rise.

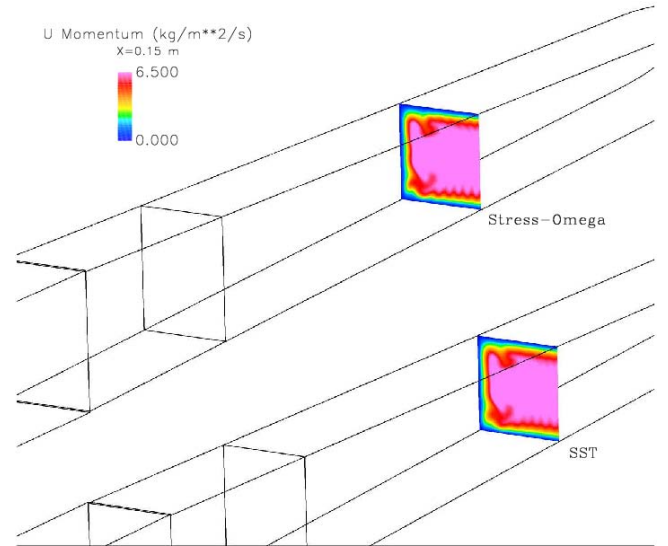


Figure 16. Comparison of the U momentum (ρu) prediction from the Stress-Omega and Menter SST simulations with a back pressure of 22.8 torr at a location just upstream of the start of the pressure rise.

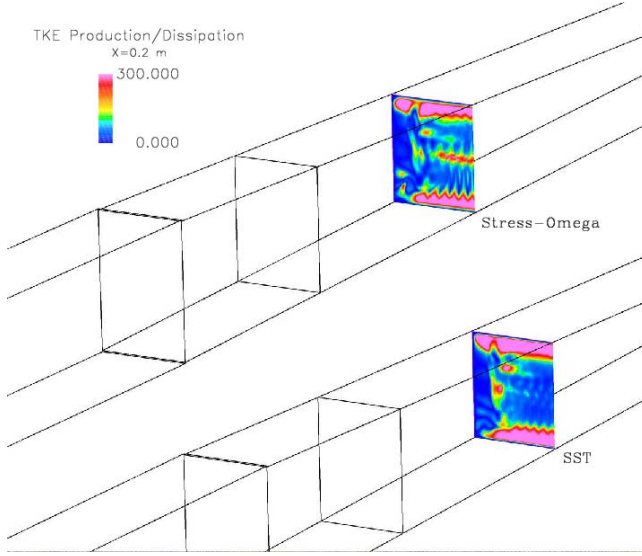


Figure 17. Comparison of the turbulent kinetic energy production to dissipation ratio predictions from the Stress-Omega and Menter SST simulations with a back pressure of 22.8 torr at a location just downstream of the start of the pressure rise.

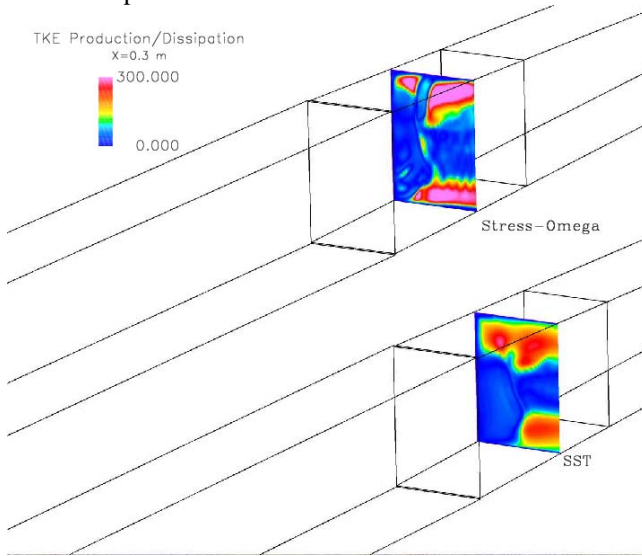


Figure 19. Comparison of the turbulent kinetic energy production to dissipation ratio predictions from the Stress-Omega and Menter SST simulations with a back pressure of 22.8 torr at a location near the end of the pressure rise.

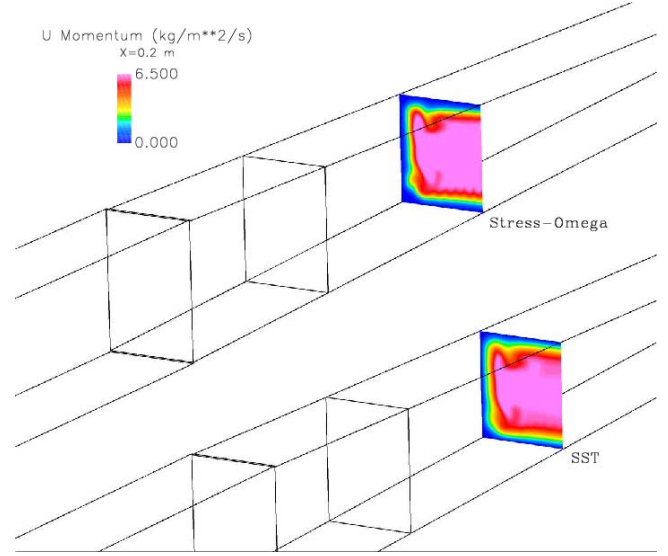


Figure 18. Comparison of the U momentum (ρu) prediction from the Stress-Omega and Menter SST simulations with a back pressure of 22.8 torr at a location just downstream of the start of the pressure rise.

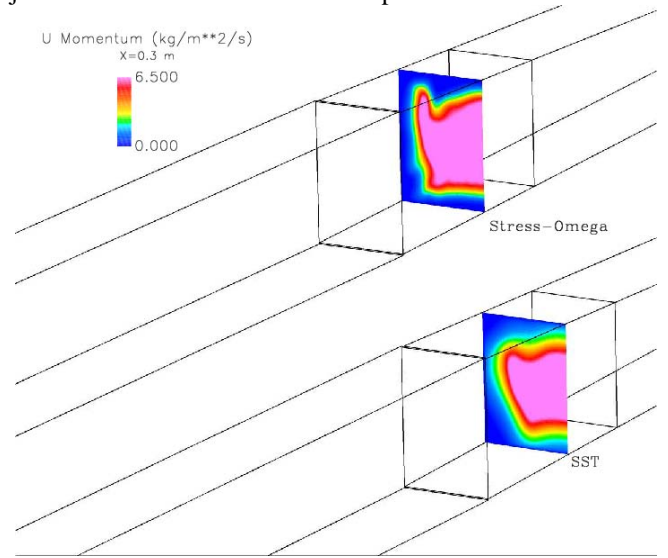


Figure 20. Comparison of the U momentum (ρu) prediction from the Stress-Omega and Menter SST simulations with a back pressure of 22.8 torr at a location near the end of the pressure rise.

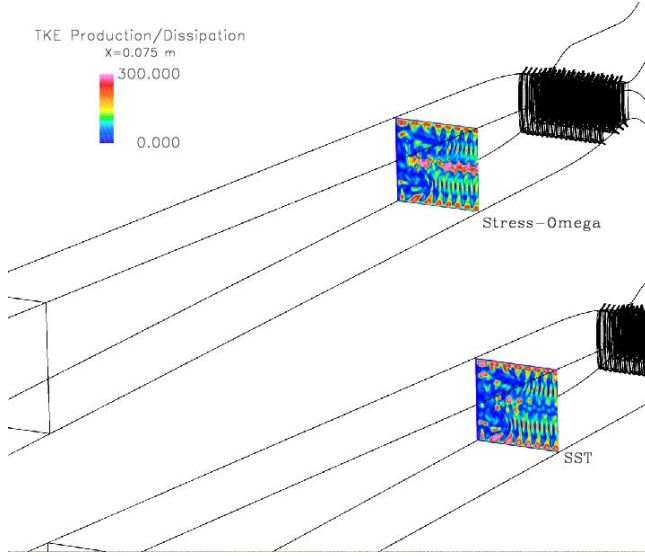


Figure 21. Comparison of the turbulent kinetic energy production to dissipation ratio predictions from the Stress-Omega and Menter SST simulations with a back pressure of 26.4 torr at a location just upstream of the start of the pressure rise.

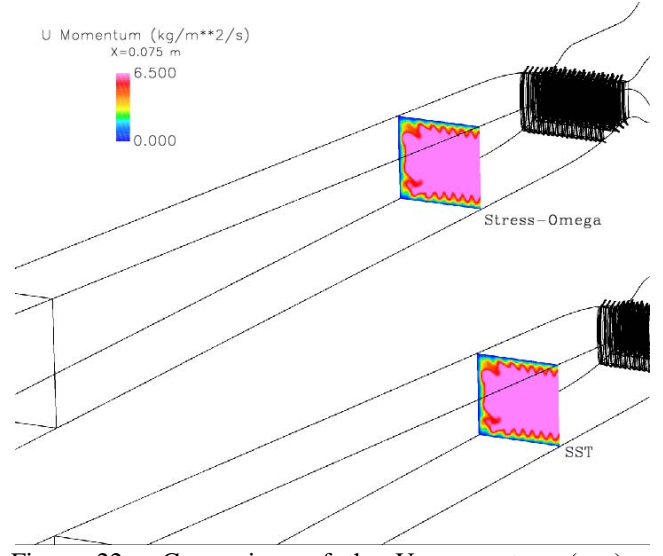


Figure 22. Comparison of the U momentum (ρu) prediction from the Stress-Omega and Menter SST simulations with a back pressure of 26.4 torr at a location just upstream of the start of the pressure rise.

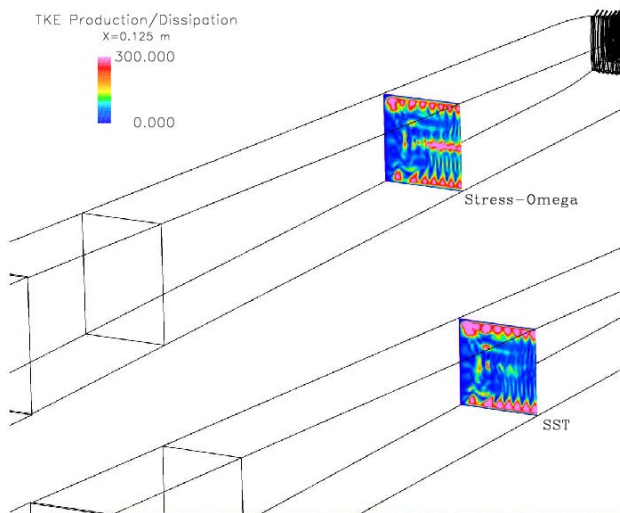


Figure 23. Comparison of the turbulent kinetic energy production to dissipation ratio predictions from the Stress-Omega and Menter SST simulations with a back pressure of 26.4 torr at a location just downstream of the start of the pressure rise.

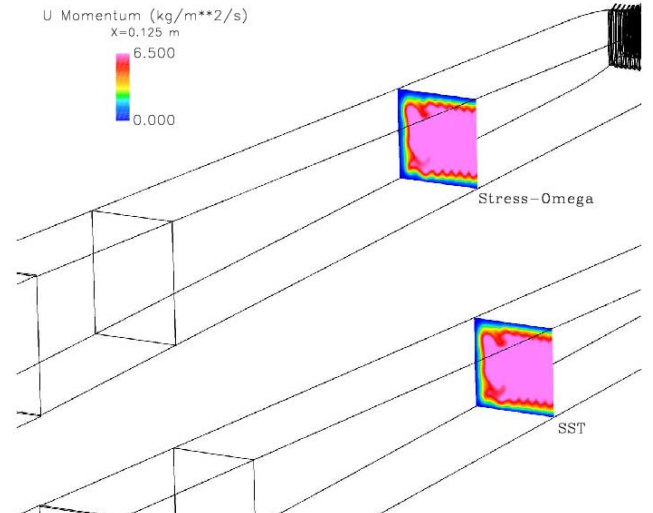


Figure 24. Comparison of the U momentum (ρu) prediction from the Stress-Omega and Menter SST simulations with a back pressure of 26.4 torr at a location just downstream of the start of the pressure rise.

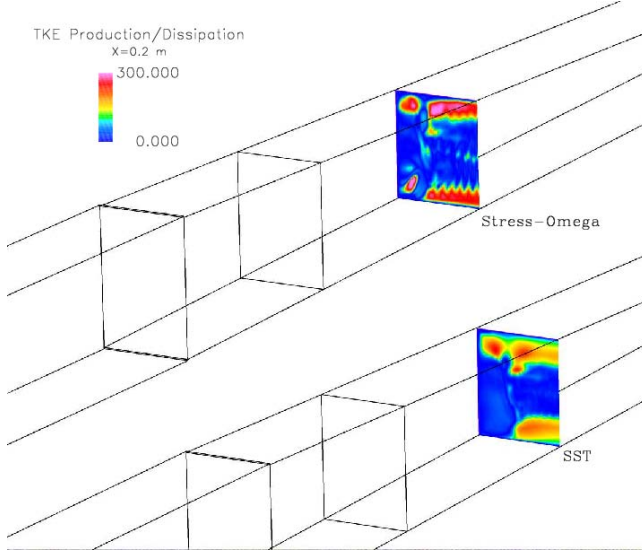


Figure 25. Comparison of the turbulent kinetic energy production to dissipation ratio predictions from the Stress-Omega and Menter SST simulations with a back pressure of 26.4 torr at a location near the end of the pressure rise.

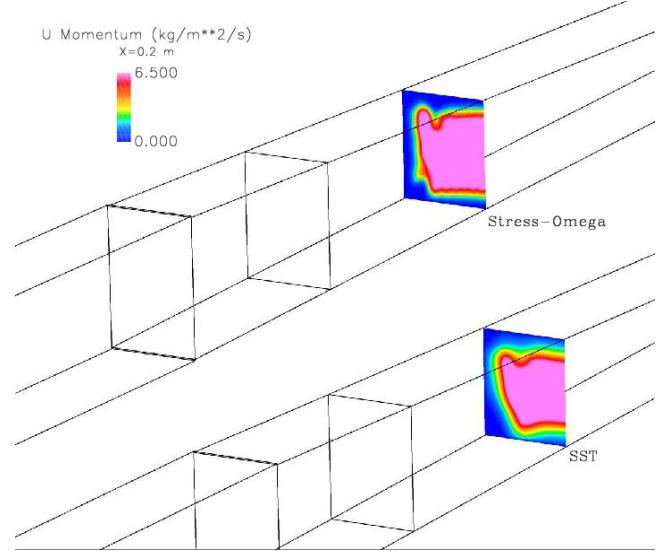


Figure 26. Comparison of the U momentum (ρu) prediction from the Stress-Omega and Menter SST simulations with a back pressure of 26.4 torr at a location near the end of the pressure rise.

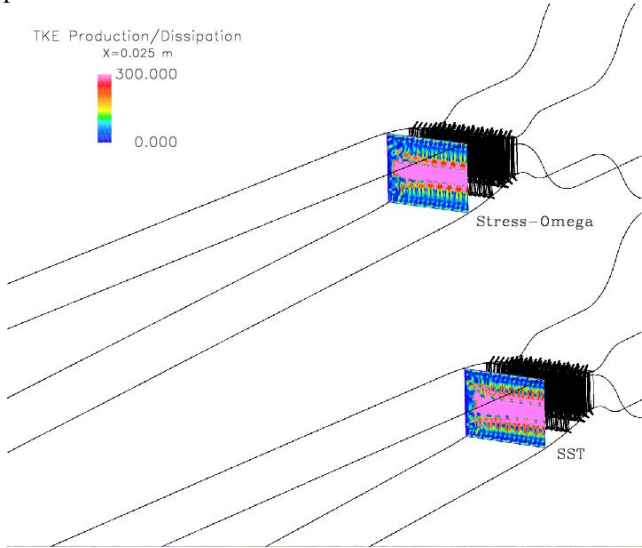


Figure 27. Comparison of the turbulent kinetic energy production to dissipation ratio predictions from the Stress-Omega and Menter SST simulations with a back pressure of 29.5 torr at a location just upstream of the start of the pressure rise.

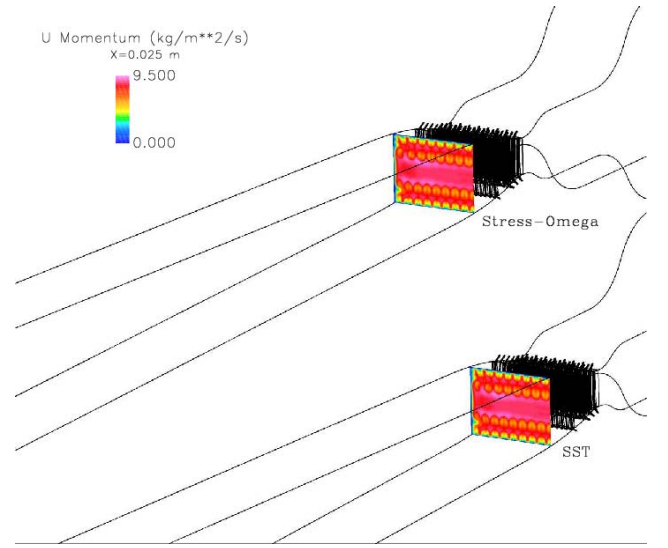


Figure 28. Comparison of the U momentum (ρu) prediction from the Stress-Omega and Menter SST simulations with a back pressure of 29.5 torr at a location just upstream of the start of the pressure rise.

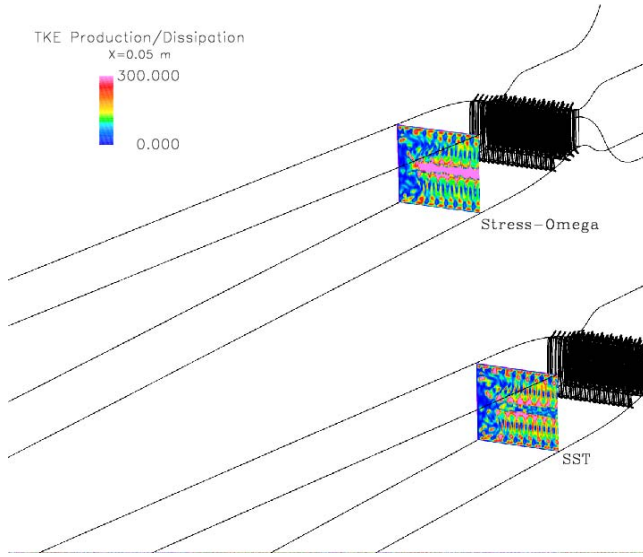


Figure 29. Comparison of the turbulent kinetic energy production to dissipation ratio predictions from the Stress-Omega and Menter SST simulations with a back pressure of 29.5 torr at a location just downstream of the start of the pressure rise.

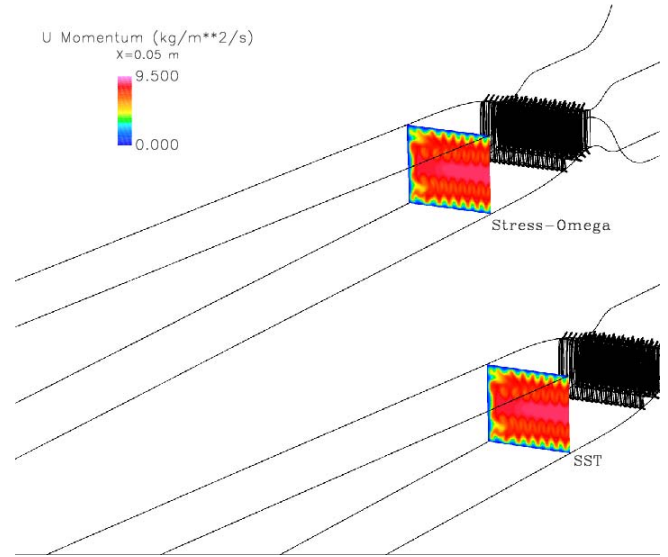


Figure 30. Comparison of the U momentum (ρu) prediction from the Stress-Omega and Menter SST simulations with a back pressure of 29.5 torr at a location just downstream of the start of the pressure rise.

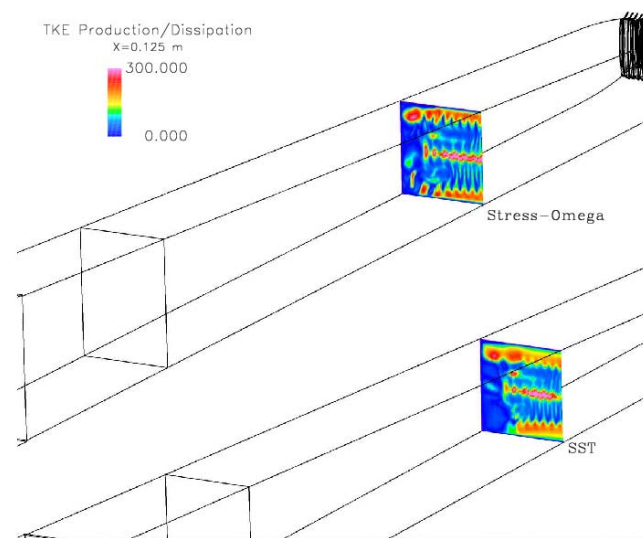


Figure 31. Comparison of the turbulent kinetic energy production to dissipation ratio predictions from the Stress-Omega and Menter SST simulations with a back pressure of 29.5 torr at a location near the end of the pressure rise.

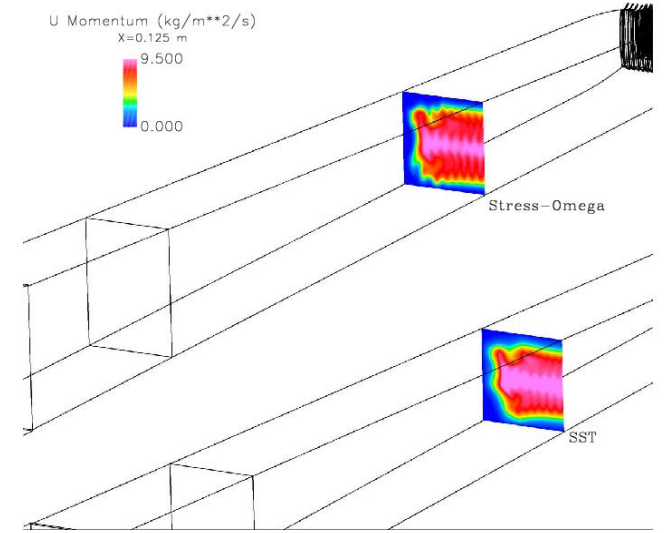


Figure 32. Comparison of the U momentum (ρu) prediction from the Stress-Omega and Menter SST simulations with a back pressure of 29.5 torr at a location near the end of the pressure rise.

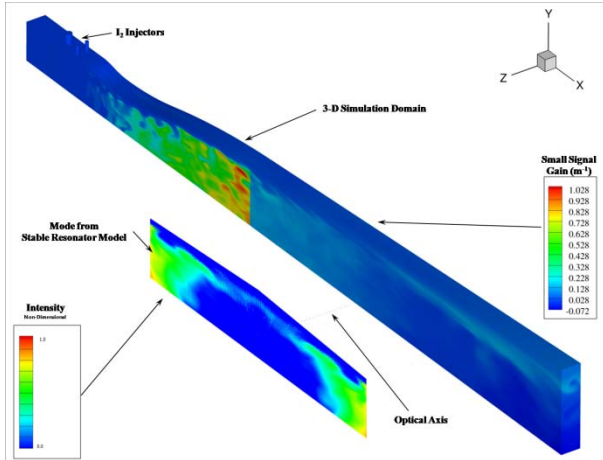


Figure 33. Laser gain and intensity from 3-D GASP simulation of a COIL mixing nozzle illustrating the connection between laser resonance and flow structure. Note that the flow structure directly influences the gain and the intensity.

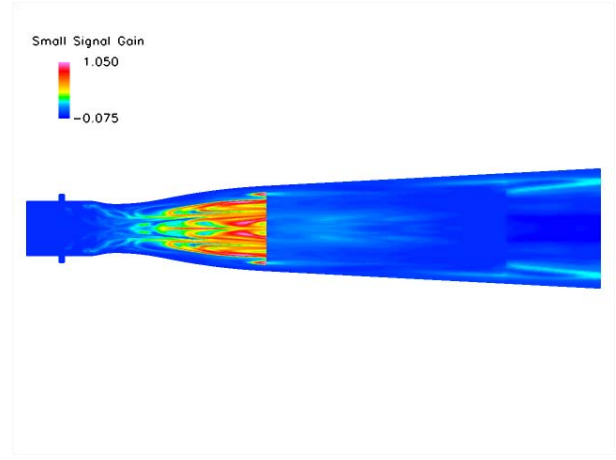


Figure 34. Laser gain distribution from the 3-D GASP simulation of a COIL mixing nozzle using a time step of $1 \cdot 10^{-3}$ sec and time step limiting. Note the decrease in gain which occurs as the flow enters the laser cavity and power is extracted from the flow. Also, compare the flow structure with that from Fig. 35.

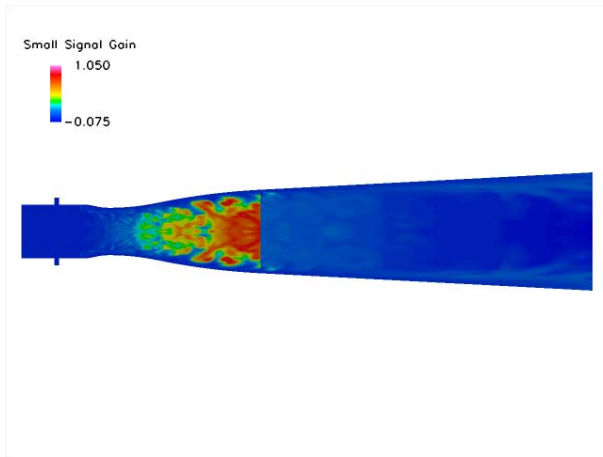


Figure 35. Laser gain distribution from the 3-D GASP time accurate simulation of a COIL mixing nozzle using a time step of $1 \cdot 10^{-8}$ sec. Note the decrease in gain which occurs as the flow enters the laser cavity and power is extracted from the flow. Also, compare the flow structure with that from Fig. 34.

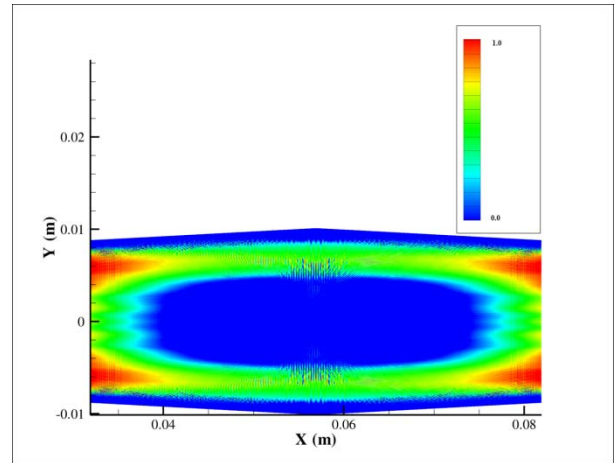


Figure 36. Laser intensity distribution from the 3-D GASP simulation of a COIL mixing nozzle using a time step of $1 \cdot 10^{-3}$ sec and time step limiting. Note how the intensity field corresponds with the gain distribution and flow structure in Fig. 34 and compare with the intensity in Fig. 37.

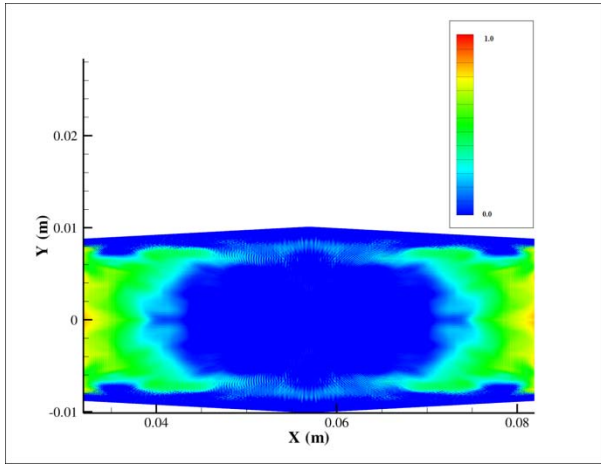


Figure 37. Laser intensity distribution from the 3-D GASP time accurate simulation of a COIL mixing nozzle using a time step of $1 \cdot 10^{-8}$ sec. Note how the intensity field corresponds with the gain distribution and flow structure in Fig. 35 and compare with the intensity in Fig. 36.

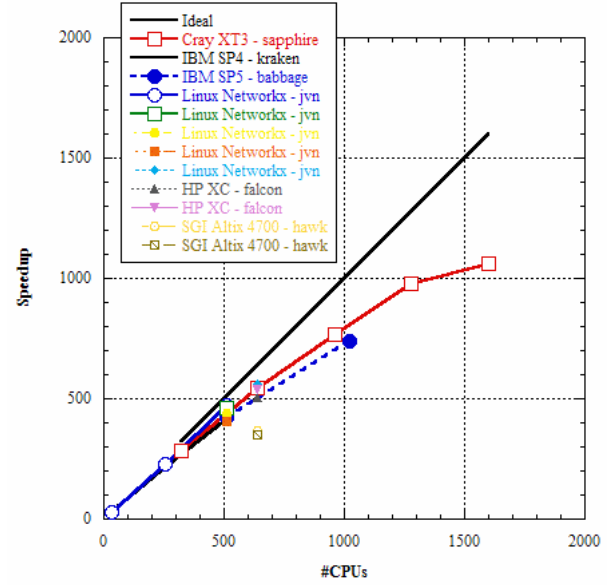


Figure 38. Speedups for GASP on various platforms. Note that the XT3 data are for a simulation using 13 species, thereby increasing the communications costs by a factor of 2.5 over a single gas simulation.

DISTRIBUTION LIST

DTIC/OCP 8725 John J. Kingman Rd, Suite 0944 Ft Belvoir, VA 22060-6218	1 cy
AFRL/RVIL Kirtland AFB, NM 87117-5776	2 cys
Official Record Copy AFRL/RDLC/Timothy J. Madden	2 cys